Energy & Environmental Science

ROYAL SOCIETY OF CHEMISTRY

PAPER

View Article Online
View Journal

Cite this: DOI: 10.1039/d6ee00199h

Molecular engineering of conjugated polymer cathodes *via* the one-pot preparation of high-rate and ultra-stable aqueous/seawater Zn-ion batteries under harsh conditions

Quanwei Ma,†[a] Cheng Ji,†[a] Zeyu Wang,[b] Rui Wang,[a] Longhai Zhang,[a] Hongbao Li,[a] Ying Xu,[c] Qianyu Zhang,[d] Dongliang Chao *[b] and Chaofeng Zhang *[a]

Organic materials are promising candidates as cathodes for high-performance aqueous Zn-ion batteries (AZIBs) owing to their high capacity, structural adjustability, and sustainability. However, their practical application is hindered by limited redox activity and low electronic conductivity under harsh operating conditions. Here, we report an organic polymer cathode prepared using a simple one-pot method, poly(mellitic trianhydride-phenazine) (PMPZ), featuring a fully conjugated structure and abundant active functional groups. The incorporation of heterocyclic conjugated units into the conjugated polymer structure enhances its electron affinity and π-electron delocalization, resulting in high redox activity and significantly elevated conductivity. Meanwhile, multiple C═O and C═N redox-active centers act cooperatively to enable a multielectron redox process through this delocalization pathway, thereby improving charge storage and reaction kinetics. Through combined theoretical and *operando* synchrotron experimental studies, we further elucidate that this fully conjugated structure facilitates reversible Zn^{2+}/H^{+} co-storage with multiple electron transfers. Consequently, the PMPZ cathode demonstrates exceptional electrochemical performance with remarkable rate capability and outstanding cycling stability across a wide temperature range from −50 °C to 50 °C, even with seawater-based electrolytes. This work provides a novel design strategy for developing high-performance AZIB cathodes capable of operating under extreme conditions.

Received 10th January 2026,
Accepted 29th April 2026

DOI: 10.1039/d6ee00199h

rsc.li/ees

Broader context

Rechargeable organic cathodes are capturing increasing attention in aqueous zinc-ion batteries (AZIBs), owing to their high theoretical capacity, sustainability, and structural designability. However, their widespread practical application poses significant challenges, primarily due to their insufficient redox activity and compromised electronic conductivity, which collectively curtail their energy density and reaction kinetics under demanding operational environments. We have designed PMPZ through molecular engineering, simultaneously addressing the major challenges related to cycling stability, operational temperature range, and energy density. Furthermore, multi-scale structural and electrochemical analyses correlated the designed architecture of PMPZ with its performance, revealing the underpinnings of its redox activity, reaction mechanism, and stability. This work thereby ushers in a paradigm shift from empirical searches to a rational design methodology for organic cathode materials.

[a] *Institutes of Physical Science and Information Technology, Leibniz International Joint Research Centre of Materials Sciences of Anhui Province, Key Laboratory of Environment-Friendly Polymeric Materials of Anhui Province, Anhui University, Hefei 230601, China. E-mail: cfz@ahu.edu.cn*

[b] *Laboratory of Advanced Materials, Aqueous Battery Center, Shanghai Key Laboratory of Molecular Catalysis and Innovative Materials, Collaborative Innovation Center of Chemistry for Energy Materials, Shanghai Wusong Laboratory of Materials Science, State Key Laboratory of Porous Materials for Separation and Conversion, College of Smart Materials and Future Energy, Fudan University, Shanghai 200433, China. E-mail: chaod@fudan.edu.cn*

[c] *School of Materials Science and Engineering, Anhui University, Hefei 230601, China*

[d] *College of Materials Science and Engineering, Sichuan University, Chengdu 610064, China*

† These authors contributed to this work equally.

Introduction

The increasing global demand for the efficient utilization and distribution of renewable energy for power generation has spurred extensive research into advanced energy storage technologies.[1–4] Rechargeable aqueous batteries are promising for grid-scale energy storage owing to their inherent safety, environmental sustainability, and low cost.[5–10] Among them, aqueous zinc-ion batteries (AZIBs) have garnered significant attention owing to the natural abundance of Zn, eco-friendliness, high theoretical capacity (820 mA h g^{-1}), and favorable redox potential

(−0.76 V *vs.* SHE).[11–15] Cathode materials are critical for achieving high performance in AZIBs. Currently, numerous inorganic cathode materials, such as Mn-based/V-based compounds and Prussian blue analogues (PBAs), have been widely explored as cathodes in these systems.[16,17] Nevertheless, the advancement of high-performance AZIBs was hampered by considerable hurdles. The Zn^{2+} ion, with a relatively high charge density (charge-to-size ratio) and strong coulombic interactions, severely hinders the diffusion kinetics within the rigid lattice frameworks of these inorganic cathodes.[18,19] Moreover, the repeated intercalation/deintercalation of Zn^{2+} frequently induces substantial structural stress, leading to irreversible structural degradation, including structural collapse and dissolution of the active material.[20,21] Consequently, these issues lead to rapid capacity fading and diminished electrochemical performance. Therefore, the exploration and development of novel cathode materials exhibiting superior structural stability and ion diffusion kinetics are crucial for high performance AZIBs.

Organic materials offer a promising alternative for AZIB cathodes due to their sustainability, high theoretical capacity, and structural designability.[18,22,23] Unlike inorganic electrodes, organic materials operate through ion-coordination mechanisms and involve reversible bond rearrangement, which enhances the structural stability and reaction kinetics of electrode materials.[24–26] However, they also present inherent drawbacks, such as poor intrinsic electronic conductivity, severe dissolution of small-molecule active species in aqueous electrolytes, relatively low operating voltages, and insufficient utilization of redox sites, all of which limit their practical applications.[25] To address these bottlenecks, conjugated organic molecules with extended π-electron structures have garnered significant interest as cathode materials due to their high conductivity and structural stability.[27] In such conjugated systems, π-electrons delocalize along the molecular backbone instead of remaining localized on individual atoms, which reduces the energy gap between the highest occupied molecular orbital (HOMO) and the lowest unoccupied molecular orbital (LUMO) levels, thereby facilitating efficient electron transport.[25,28] Despite remarkable improvements in structural stability and electronic conductivity over small molecules, π-conjugated polymers still suffer from critical drawbacks, including the introduction of electrochemically inactive linkages and rigid conjugated backbones, which reduce active-site density and impede Zn^{2+} storage.[29,30] This phenomenon presents a key challenge for AZIBs, achieving both high activity and sufficient electronic conductivity in organic cathodes. Therefore, the development of novel conjugated organic cathodes is crucial for achieving high-performance AZIBs with high rate capability and extended cycle life under harsh operating conditions.

Here, we designed and synthesized a novel fully conjugated organic polymer (PMPZ) through a one-step Friedel–Crafts reaction between phenazine (PNZ) and mellitic trianhydride (MT) (Fig. 1a). The PMPZ polymer achieves significantly greater π-electron delocalization along the molecular backbone by integrating heterocyclic conjugated units, which improves electronic conductivity and strengthens electron affinity. Furthermore, multiple C═O and C═N active groups work synergistically within the delocalized electronic structure to facilitate efficient

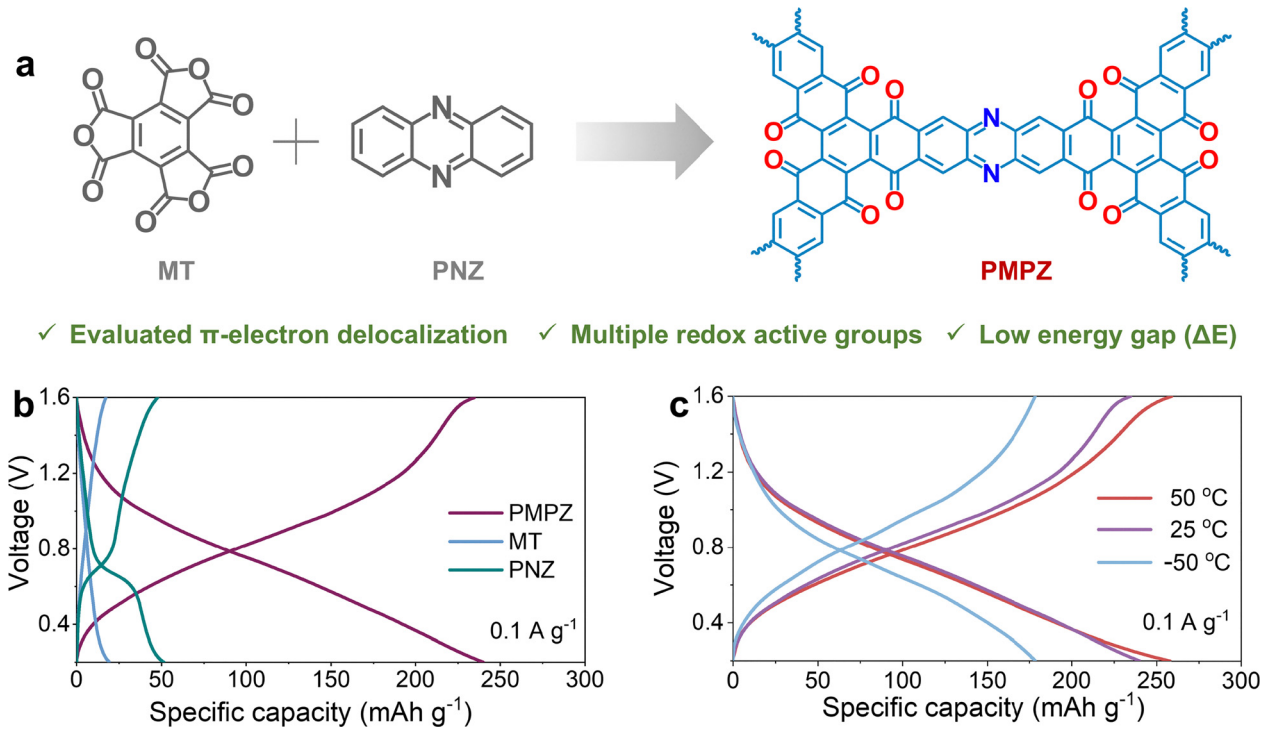

Fig. 1 (a) Synthesis diagram of PMPZ. (b) Charge/discharge curves of MT, PNZ, and PMPZ at 0.1 A g^{-1}. (c) Charge/discharge curves of PMPZ at 0.1 A g^{-1} at 50 °C, 25 °C, and −50 °C.

multi-electron transfer processes, enhancing charge storage capability and ensuring fast reaction kinetics at different temperatures. Consequently, when used as the cathode for AZIBs, the PMPZ cathode delivers a high capacity of 240 mA h g^{-1} at 0.1 A g^{-1}, exceptional rate capability of 179 mA h g^{-1} at 50 A g^{-1}, and outstanding cycling stability of over 60 000 cycles. Benefiting from its unique structure, the PMPZ cathode shows remarkable electrochemical performance across a wide temperature range from 50 °C to −50 °C (Fig. 1b and c). It delivers a high capacity of 260 mA h g^{-1} and 175 mA h g^{-1} at 0.1 A g^{-1} when operated at 50 °C and −50 °C, respectively, and demonstrates exceptional cycling stability over 10 000 cycles at both temperatures. Even in a seawater-based electrolyte, the PMPZ cathode exhibits a high capacity of 223 mA h g^{-1} at 0.1 A g^{-1} and maintains stable performance over 5000 cycles. This work offers valuable insights for developing organic cathode materials suited to high-performance AZIBs under harsh conditions.

Results and discussion

Synthesis and characterizations

The PMPZ polymer was synthesized by a one-step Friedel–Crafts reaction between phenazine (PNZ) and mellitic trianhydride (MT) (Fig. 1a). The chemical structure of the as-prepared PMPZ was characterized by Fourier transform infrared (FT-IR), X-ray photoelectron spectroscopy (XPS), and ^{13}C solid-state nuclear magnetic resonance (^{13}C SSNMR) spectroscopy. As depicted in Fig. 2a, the FT-IR spectrum of PMPZ confirms the presence of C═O and C═N functional groups, as evidenced by the characteristic stretching vibrations at 1675 cm^{-1} and 1542 cm^{-1}, respectively.[27,31] Additionally, the anhydride bonds at 1850 cm^{-1} disappeared in the FT-IR spectrum of PMPZ compared to that of MT, indicating that anhydride bonds were involved in the reaction. Moreover, the peaks at 138 and 165 ppm in the ^{13}C SSNMR spectrum of PMPZ confirm the presence of C═N and C═O within the molecular structure (Fig. 2b).[32,33] Notably, the broad characteristic peaks in the range from110 to 135 ppm of the ^{13}C SSNMR spectrum likely arise from overlapping C═C peaks from the aromatic rings of the polymer.[34] XPS analysis of PMPZ confirms that its chemical composition consists primarily of C, N, and O without detectable impurities, as shown in the survey XPS spectrum (Fig. S1a). The C 1s spectrum unambiguously confirms the presence of C═N (286.3 eV), C═O (288.7 eV), and C–N (285.2 eV) in PMPZ (Fig. S1b).[18,35] Consistent with these findings, the deconvoluted N 1s and O 1s spectra (Fig. S1c and d) exhibit characteristic peaks of C═N, C═O, and C–N species, which corroborates the results in the C 1s spectrum. Notably, although both the C 1s and O 1s spectra of MT show a dominant C–O peak (Fig. S2), this peak feature is absent in PMPZ. This result provides direct evidence that the anhydride moiety participated in the reaction, leading to the generation of C═O bonds in PMPZ.

Furthermore, XRD analysis (Fig. S3) shows a broad peak at approximately 26.1° for the PMPZ polymer, which contrasts with the sharp crystalline peaks of its monomers and indicates π–π stacking between the aromatic units. The non-covalent interactions within the PMPZ polymer were further probed by a reduced density gradient (RDG) analysis, which reveals green spikes in the region where the sign(λ_2)ρ ranges from −0.02 to 0.00 (Fig. 2c), demonstrating π–π interactions between adjacent polymer molecules.[16,36,37] These vertically oriented interactions facilitate highly efficient interfacial charge transfer and enhance redox reaction kinetics in the PMPZ polymer.[38,39] The thermogravimetric analysis (TGA) curve indicates that PMPZ exhibits excellent thermal stability, with no significant mass loss until the temperature exceeds 400 °C (Fig. 2d). This exceptional stability arises from strong intramolecular π–π coupling, which delocalizes electronic charge and reduces thermal decomposition reactivity. Consequently, these interactions ensure structural persistence during electrochemical cycling.

As shown in Fig. 2e, molecular electrostatic potential (ESP) simulations reveal pronounced negative potential regions localized at the C═O and C═N groups, illustrating these sites as electrochemically active centers for cation coordination.[40] In addition, the calculated highest occupied molecular orbital (HOMO) and the lowest unoccupied molecular orbital (LUMO) for PMPZ are presented in Fig. 2f. Frontier molecular orbital analysis shows that the LUMO of PMPZ is at −5.21 eV, which is significantly lower than that of conventional organic electrodes (*e.g.*, PNZ: −3.76 eV). This decreased LUMO energy correlates with enhanced electron affinity and a positive shift in reduction potential, confirming superior redox activity.[41,42] Crucially, PMPZ exhibits an ultranarrow HOMO–LUMO gap of 0.33 eV, substantially reduced *versus* those of MT (2.29 eV) and PNZ (1.56 eV), indicating facilitated interorbital electron transitions and intrinsic charge delocalization across the conjugated framework.[27,28] Moreover, the π-electronic distribution of PMPZ was visualized using the π-electron localized orbital locator (LOL-π) (Fig. 2g) to analyze structural stability through the extent of π-conjugation. The LOL-π analysis reveals well-distributed π-electrons across the C═C, C═N, and C═O frameworks, revealing an uninterrupted π-conjugation pathway that extends the delocalized range.[31] This enhanced electronic delocalization fundamentally underpins the favorable structural stability of the polymer. Beyond LOL-π analysis, aromaticity is a key metric for evaluating the structural stability of organic compounds. As shown in Fig. 2h, the positive Harmonic Oscillator Model of Aromaticity (HOMA) values for all rings in PMPZ confirm its outstanding aromatic character, indicating enhanced global aromaticity and structural stability, which ensures excellent cycling stability.[43]

Furthermore, diffuse reflectance ultraviolet-visible-near-infrared (DRUV-vis-NIR) spectroscopy reveals a broad absorption peak centered around 800 nm (Fig. 2i) for PMPZ, which can be attributed to extended conjugation within its polymer backbone. Notably, PMPZ shows a distinctive mid-infrared absorption tail, signifying a more expansive delocalized electronic structure and enhanced intermolecular charge transfer relative to MT and PNZ.[44] Owing to this favourable molecular architecture, PMPZ achieves a narrow optical bandgap of 0.89 eV (Fig. 2j), significantly lower than that of PNZ (2.73 eV) and

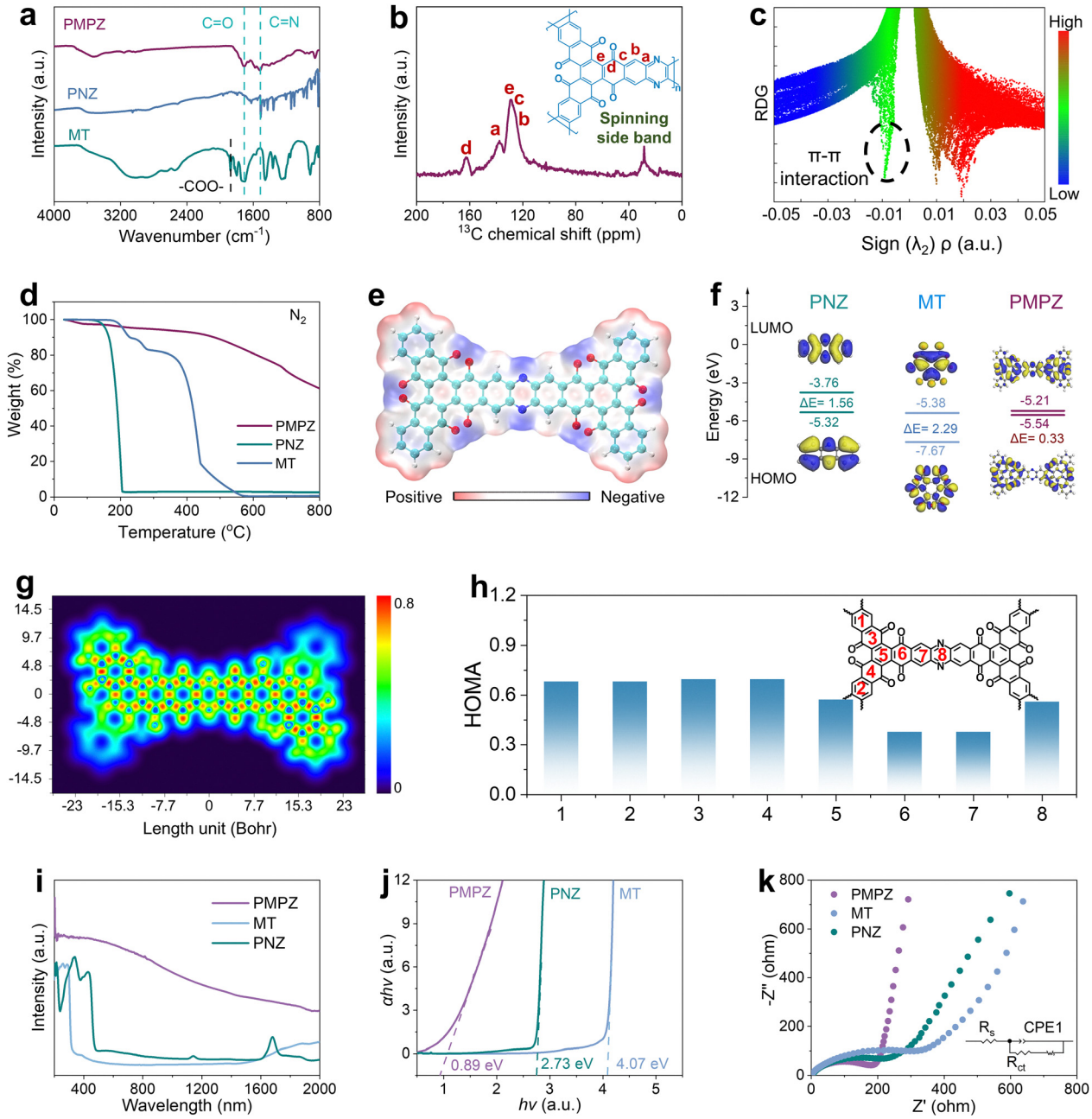

Fig. 2 (a) FT-IR spectra of MT, PNZ, and PMPZ. (b) Solid-state ^{13}C NMR spectrum of PMPZ. (c) Plots of reduced density gradient *vs.* sign (λ_2) ρ of PMPZ. (d) TGA curves of MT, PNZ, and PMPZ under N_2. (e) Optimized geometries and ESP image of PMPZ. (f) Calculated HOMO/LUMO energies of MT, PNZ, and PMPZ. (g) LOL-π image of the PMPZ molecule. (h) Calculated HOMA values of PMPZ. (i) DRUV-vis-NIR spectra of MT, PNZ, and PMPZ. (j) Optical energy gaps of MT, PNZ, and PMPZ. (k) EIS plots of MT, PNZ, and PMPZ (inset: equivalent circuit model).

MT (4.07 eV). The reduced bandgap endows PMPZ with enhanced electronic conductivity and rapid charge transport capabilities, facilitating high redox reaction kinetics.[17] Moreover, the temperature-dependent electronic conductivity of PMPZ was further investigated (Fig. S4). The conductivity increases with rising temperature, reaching 2.83×10^{-6} S cm^{-1} at −100 °C, 5.26×10^{-6} S cm^{-1} at room temperature, and 7.25×10^{-6} S cm^{-1} at 100 °C, which guarantees its outstanding electrochemical performance over a wide temperature range. Notably, the electronic conductivity of PPP is far superior to that of most reported organic cathode materials,[45] indicating that such heterocyclic fully conjugated polymers remarkably promote charge transport. Electrochemical impedance spectroscopy (EIS) further corroborates these findings, as shown in Fig. 2k. The EIS plots of PMPZ feature a semicircle with a Warburg tail, revealing a significantly lower charge transfer resistance (R_{ct}) of PMPZ (152 Ω) compared to MT (284 Ω) and PNZ (202 Ω). This reduced R_{ct} reflects enhanced electronic conductivity, resulting from the extended conjugated structure, which is consistent with the theoretical calculation results.

The activation energy (E_a) for interfacial charge transfer in the PMPZ cathode was calculated by fitting electrochemical impedance spectroscopy data (Fig. S5). According to the Arrhenius equation, the ion-storage process in PMPZ exhibits a low E_a of merely 0.20 eV, considerably lower than those of MT (0.25 eV) and PNZ (0.22 eV). Such a reduced activation energy barrier directly verifies that the heteroatom-doped fully conjugated structure effectively enables fast charge transfer kinetics and redox reactions in the PMPZ cathode. It substantially lowers the reaction energy threshold, allowing ions and charges to readily access and interact with redox-active sites throughout the electrode.[17]

Electrochemical performance

The electrochemical performance of PMPZ as an AZIB cathode was evaluated using a coin-type cell with a Zn foil anode and 3 M $Zn(ClO_4)_2$ electrolyte. As shown in Fig. 3a, cyclic voltammetry (CV) was performed to study the redox behavior of PMPZ at 0.1 mV s^{-1}. The CV curve of PMPZ features two reversible redox couples (0.76/0.71 and 0.52/0.44 V), assigned to the C═O

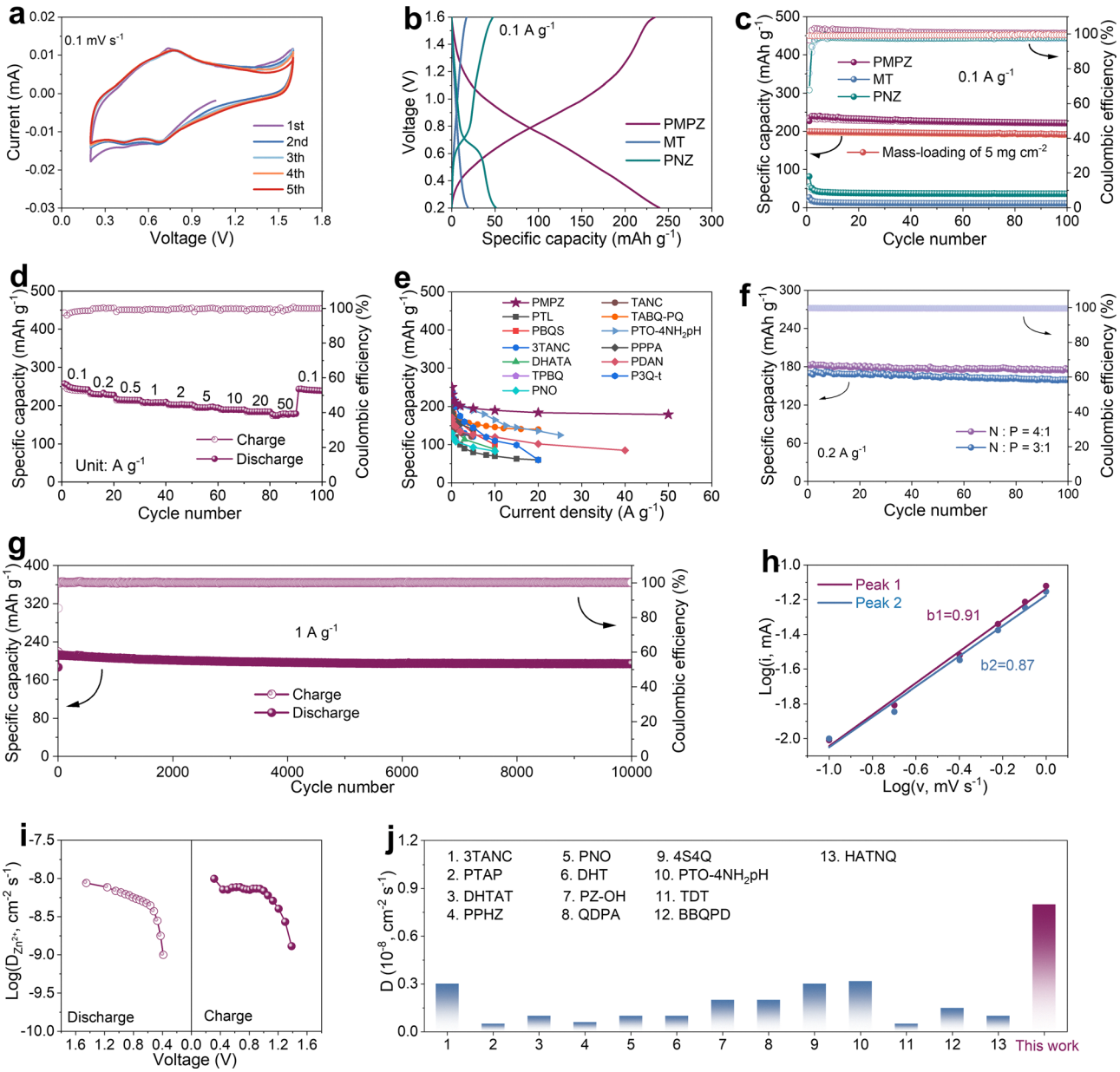

Fig. 3 Electrochemical performance of the PMPZ cathodes for AZIBs. (a) CV curves of PMPZ at 0.1 mV s^{-1}. (b) Charge/discharge curves of PMPZ, MT, and PNZ at 0.1 A g^{-1}. (c) Cycling performance of PMPZ with low mass loading and high mass loading of 5 mg cm^{-2} with those of MT and PNZ at 0.1 A g^{-1}. (d) Rate performance of PMPZ at different current densities. (e) Rate performance comparison among PMPZ and other reported organic cathodes. (f) Cycling performance of PMPZ with N/P ratios of 3 : 1 and 4 : 1 at 0.2 A g^{-1}. (g) Long-term cycling performance of PMPZ at 1 A g^{-1}. (h) Corresponding log (*i*) *vs.* log (*v*) curves of the PMPZ cathode. (i) Zn^{2+} diffusion coefficients of the PMPZ cathode at different discharge/charge states. (j) Comparison of D_{Zn}^{2+} among PMPZ and various previously reported cathodes.

and C═N functional groups, respectively (Fig. S6a). After the first cycle, the PMPZ cathode shows stable and reversible CV curves, indicating good electrochemical reversibility. Subsequent galvanostatic charge/discharge tests reveal that the extended conjugated structure induces extensive π-electron delocalization, leading to an elevated redox potential (Fig. 3b and Fig. S6b).[27] The combination of an improved voltage plateau and multi-electron redox processes collectively boosts capacity and energy density. As shown in Fig. 3c and Fig. S7a, the PMPZ cathode displays a high capacity of 240 mA h g^{-1} at 0.1 A g^{-1} and maintains 92.7% of its initial capacity after 100 cycles. In comparison, the MT and PNZ cathodes show low capacity (27 and 82 mA h g^{-1}, respectively) with poor capacity retention (41% for MT and 46% for PNZ), as depicted in Fig. S7b and c. In addition, when the PMPZ loading is 5 mg cm^{-2}, the PMPZ cathode achieves a discharge capacity of 201 mA h g^{-1} at 0.1 A g^{-1}, and the capacity retention rate is 94% after 100 cycles, which fully verifies that PMPZ can maintain excellent electrochemical performance even under high loading conditions (Fig. 3c and Fig. S7d).

Fig. 3d and Fig. S8a demonstrate the rate performance of PMPZ at different current densities. Specifically, the PMPZ cathode exhibits high specific capacities of 248, 231, 215, 208, 202, 195, 190, 185, and 179 mA h g^{-1} at 0.1, 0.2, 0.5, 1, 2, 5, 10, 20, and 50 A g^{-1}, respectively. Upon reverting the current density to 0.1 A g^{-1}, the capacity recovered to 239 mA h g^{-1}, illustrating exceptional rate capability and excellent reversibility of PMPZ. Moreover, PMPZ displays similarly shaped charge/discharge curves with minimal voltage polarization across various current densities, confirming rapid reaction kinetics. Importantly, the PMPZ cathode outperforms most reported organic cathodes (Fig. 3e).[16,27,29,31,34,43,46–51] The excellent rate capability of PMPZ primarily originates from its fully conjugated structure and strong electronegative groups (C═O and C═N), thereby improving charge transfer and ion storage capability. Furthermore, the Zn//PMPZ pouch cell can power LED lights and keep the LED lights working under bending conditions, highlighting its potential as a viable candidate for advanced electronic devices (Fig. S9). To better demonstrate the practical application potential of the PMPZ cathode, we further evaluated the Zn//PMPZ cells with N/P ratios of 3 : 1 and 4 : 1. As shown in Fig. 3f, the Zn/PMPZ batteries delivered reversible capacities of 161 and 174 mA h g^{-1} at the N/P ratios of 3 : 1 and 4 : 1, respectively, after 100 cycles. The excellent performance of PMPZ underscores the advantages of its molecular architecture. Remarkably, the PMPZ cathode demonstrates outstanding long-term cycling stability, delivering a capacity of 194 mA h g^{-1} (91% retention) after 10 000 cycles at 1 A g^{-1} (Fig. 3g). Notably, PMPZ can maintain well-defined discharge/charge curves at 1 A g^{-1} even after 10 000 cycles (Fig. S8b). Given its outstanding rate performance, the prolonged cycling performance of PMPZ was further investigated at 20 A g^{-1}. The PMPZ cathode demonstrates exceptional cycling stability over 60 000 cycles, while maintaining a capacity of 161 mA h g^{-1} with 88% retention (Fig. S10). Importantly, a single charge/discharge cycle can be completed in approximately one minute, meeting the requirements for ultrafast energy storage. The exceptional cycle performance of PMPZ is primarily attributed to its structural stability enabled by π–π stacking interactions. A comparative analysis with reported organic cathodes for AZIBs further demonstrates the superior performance of PMPZ (Table S1).

The CV curves show well-defined reversible redox couples (Fig. S11) at scan rates ranging from 0.1 to 1 mV s^{-1}, with a slight polarization broadening observed at higher scan rates. For the PMPZ cathode, the *b*-values for peaks *b*1 (0.91) and *b*2 (0.87) (Fig. 3h) are between 0.5 and 1.0. The analysis of the *b*-values reveals that PMPZ exhibits a hybrid charge storage process involving both surface-controlled pseudo-capacitance and diffusion-controlled processes.[40,52] The Zn^{2+} diffusion coefficients for PMPZ were calculated to be in the range of 10^{-8}–10^{-9} cm^2 s^{-1} (Fig. 3i and Fig. S12). These values exceed those of most reported organic cathodes (Fig. 3j), indicating superior ion transport kinetics.[27–29,33,39,43,46,47,53–56] The high diffusion coefficients originate from the extensive π-conjugated structure of PMPZ, which facilitates electron delocalization and enables efficient charge transfer along the polymer chains.[57] In summary, the exceptional electrochemical performance of PMPZ originates from a combination of dominant capacitive contributions, facile ion-insertion kinetics, and highly reversible redox reactions at the cathode.

Charge storage mechanism

The *operando* synchrotron FT-IR was used to track the dynamic changes of functional groups during the charge/discharge process to elucidate the charge storage mechanism of PMPZ (Fig. 4a). The pristine material exhibits characteristic vibrational peaks for C═O (1675 cm^{-1}) and C═N (1542 cm^{-1}). During discharging, the intensity of both the C═O and C═N peaks progressively decreased (Fig. 4a), which is attributed to the coordination of cations (Zn^{2+} and H^+) with C═O and C═N groups, consuming these active groups.[58,59] The subsequent charging process fully restored the original spectral features, confirming the high reversibility of this transformation. Additionally, *ex situ* XPS analysis further corroborates the storage mechanism during discharging/charging (Fig. 4b–d). In the O 1s spectrum (Fig. 4b), discharging to 0.2 V led to a decrease in the C═O peak intensity (532.2 eV) and the concomitant emergence of a peak at 533.9 eV, which is assigned to the C–O species formed *via* the oxygen-cation (Zn^{2+} and H^+) coordination. Upon full charging to 1.6 V, the C═O peak intensity recovered to its initial level, demonstrating its regeneration. Analogous reversible behavior was observed for the nitrogen species (Fig. 4c). In the N 1s spectrum, the discharge process induces a decrease in intensity of the C═N peak (398.5 eV) and a concurrent increase in the C–N peak (401.6 eV), whereas charging results in the opposite evolution, with a reduced C–N peak intensity and a recovered C═N peak intensity. Notably, the N 1s peaks exhibit an overall right shift, which can be ascribed to the increased electron density surrounding nitrogen atoms during the charge and discharge processes, leading to a shift in the N 1s binding energy.[16,38,46] Collectively, the FT-IR and XPS results illustrate the reversible redox interconversion

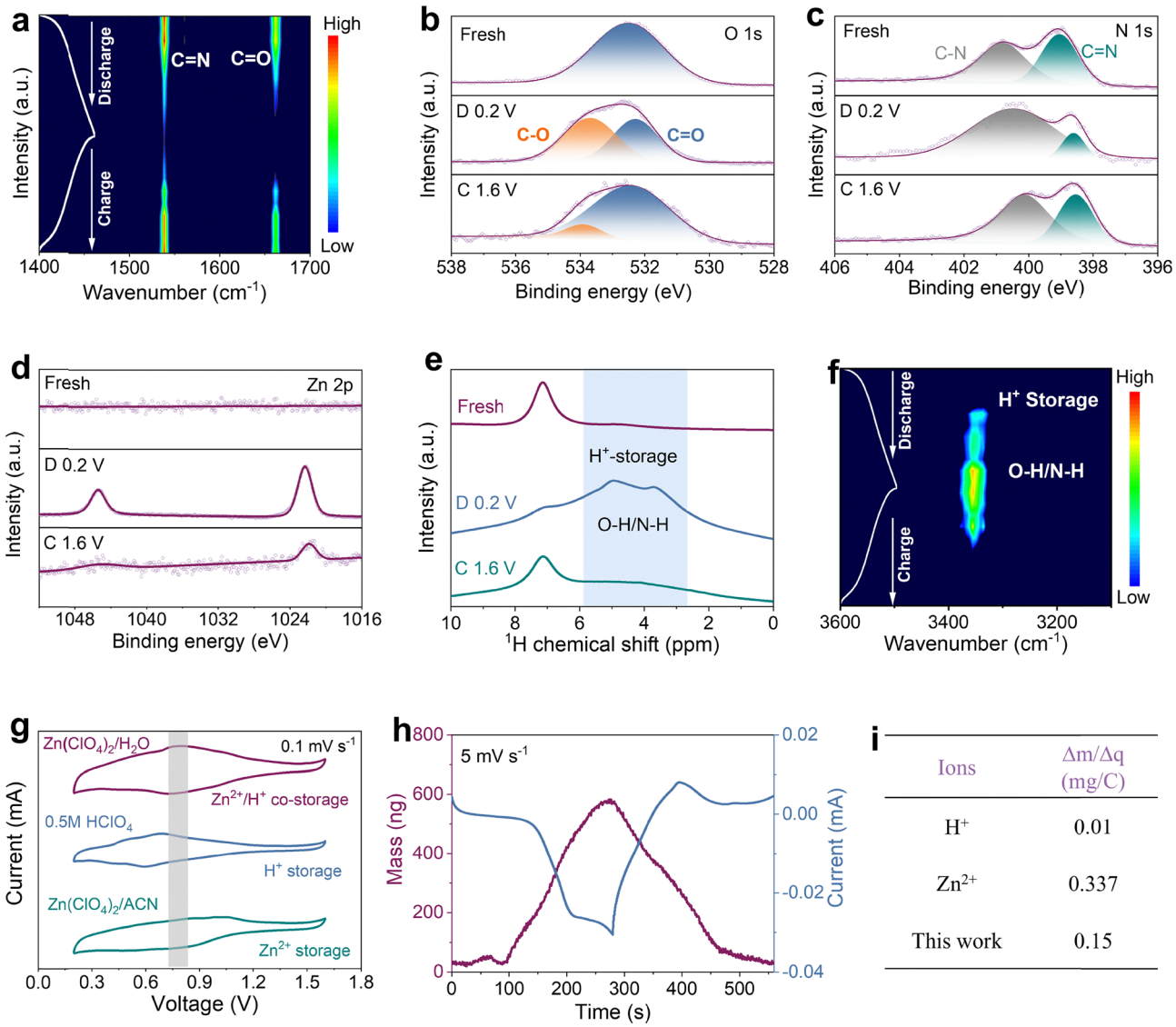

Fig. 4 (a) Charge/discharge curves of PMPZ at a current density of 0.1 A g^{-1} and *operando* synchrotron FT-IR spectra of PMPZ during the charge/discharge processes. *Ex situ* XPS spectra of (b) O 1s, (c) N 1s and (d) Zn 2p regions of the PMPZ cathode at different charge/discharge states. (e) ^{1}H SSNMR spectra of the PMPZ cathode at different charge/discharge states. (f) *Operando* synchrotron FT-IR spectra of PMPZ during the charge/discharge processes. (g) CV curves of PMPZ in different electrolytes. (h) Mass change and CV curves of PMPZ in the $Zn(ClO_4)_2/H_2O$ electrolyte. (i) $\Delta m/\Delta q$ values of H^+, Zn^{2+}, and PMPZ at 5 mV s^{-1}.

between C═O/C═N and their coordinated counterparts (C–O/C–N). Furthermore, the Zn 2p spectra (Fig. 4d) reveal a significant increase in Zn content at the discharged state and a corresponding decrease upon charging, which directly demonstrates the reversible reaction of Zn^{2+} with the PMPZ polymer.

Notably, aqueous electrolytes containing Zn^{2+} salts (*e.g.*, $Zn(ClO_4)_2$, $Zn(OTF)_2$, and $ZnSO_4$) inherently contain significant H^+ concentrations due to the unavoidable Zn^{2+} hydrolysis.[60] Therefore, to elucidate the energy storage mechanism of the PMPZ cathode, the involvement of protons (H^+) was investigated in addition to Zn^{2+} storage. *Ex situ* ^{1}H SSNMR was conducted to probe the H^+ storage behavior during the electrochemical process. As displayed in Fig. 4e, the emergence of new peaks in the 2.0–5.0 ppm region in the ^{1}H SSNMR spectra upon discharging to 0.2 V corresponds to an H^+ uptake by the PMPZ electrode, which confirms the insertion of H^+. When the PMPZ cathode was charged back to 1.6 V, the ^{1}H SSNMR spectra reverted to their original state, demonstrating the high reversibility of H^+ insertion and extraction. Complementary evidence was provided by *operando* synchrotron FT-IR spectroscopy (Fig. 4f). Discharge to 0.2 V led to the appearance of new absorption bands in the 3300–3400 cm^{-1} range, characteristic of N–H/O–H stretching vibrations, which result from the protonation of C═N/C═O functional groups. The peak diminished upon charging, reaffirming the reversible nature of H^+ storage. Together, these spectroscopic analyses consistently attest to the reversible co-storage of Zn^{2+} and H^+ in the PMPZ cathode, underscoring its dual-ion charge storage mechanism.

Moreover, to further investigate the contribution of H^+ to charge storage, we analyzed the electrochemical behavior of PMPZ in distinct electrolytes, including 3 M $Zn(ClO_4)_2/H_2O$, 3 M $Zn(ClO_4)_2$/ACN, and 0.5 M $HClO_4/H_2O$ electrolytes. As shown in the CV curves (Fig. 4g), PMPZ exhibits similar redox characteristics in both 0.5 M $HClO_4/H_2O$ electrolyte (without Zn^{2+}) and 3 M $Zn(ClO_4)_2$/ACN electrolyte (without H^+), which is consistent with the behavior observed in the 3 M $Zn(ClO_4)_2/H_2O$ electrolyte, demonstrating its ability to store both H^+ and Zn^{2+} ions. Crucially, the corresponding charge/discharge curves reveal H^+ storage capacities of 171 mA h g^{-1} in the $HClO_4/H_2O$ electrolyte and Zn^{2+} storage capacities of 149 mA h g^{-1} in the $Zn(ClO_4)_2$/ACN electrolyte. Both values are significantly lower than the 241 mA h g^{-1} achieved by the $Zn(ClO_4)_2/H_2O$ electrolyte containing both ions (Zn^{2+} and H^+) (Fig. S13). This performance disparity is directly attributable to the absence of the complementary ion in each single-ion system, providing compelling evidence for a synergistic Zn^{2+}/H^+ co-storage mechanism within the PMPZ cathode.

Subsequently, *in situ* electrochemical quartz crystal microbalance with dissipation monitoring (EQCM-D) was employed to track real-time mass and viscoelastic changes in PMPZ cathodes during CV scans (Fig. 4h and Fig. S14, S15) to further investigate the doping mechanism of PMPZ during the redox reaction. During the discharge process, the PMPZ cathode undergoes reduction, absorbing Zn^{2+} and H^+ cations from the electrolyte to maintain charge balance, leading to an increase in mass and a corresponding decrease in frequency (f_3) of the crystal. During the subsequent charging process, PMPZ is oxidized, leading to a decrease in cathode mass due to the expulsion of cations and resulting in an increase in f_3. Notably, the dissipation factor (D_3) remained virtually constant throughout the cycle, indicating minimal viscoelastic changes and preservation of a rigid polymer structure. After a full cycle, both the frequency and dissipation response recover to their initial values, confirming the high reversibility of the cation doping/dedoping processes in the PMPZ cathodes. Moreover, the mass change per charge transfer ($\Delta m/\Delta q$) was computed to determine the charge and mass transfer processes (Fig. 4h and i). In the $Zn(ClO_4)_2/H_2O$ electrolyte, the calculated $\Delta m/\Delta q$ is 0.15 mg C^{-1}. This value is significantly lower than the theoretical mass change expected for exclusive Zn^{2+} insertion/extraction (0.337 mg C^{-1}) but higher than that for exclusive H^+ transfer (0.01 mg C^{-1}). This intermediate value provides direct evidence for the concurrent participation of both Zn^{2+} and H^+ ions in the charge storage process, conclusively demonstrating the Zn^{2+}/H^+ co-storage mechanism in PMPZ.

Electrochemical performance under a wide temperature range

To comprehensively assess the practical applicability and performance advantages of the PMPZ cathode, its electrochemical performance was evaluated across a wide temperature range (50 °C, 25 °C, and −50 °C) in 3 M $Zn(ClO_4)_2$ electrolyte. Prior to low-temperature testing, cathodes were activated by 10 cycles at room temperature (RT).

As shown in Fig. 5a, the EIS plots for PMPZ feature a semicircle and a subsequent low-frequency Warburg impedance, indicating diffusion through a semi-infinite medium.[1] The linear region in the Nyquist plots indicates the Warburg diffusion impedance (Z_w), reflecting Zn^{2+} diffusion kinetics within the cathode, while the semicircle diameter relates to R_{ct}. The fitting results demonstrate consistently low R_{ct} and Z_w across all temperatures, indicating rapid charge transfer and ion diffusion kinetics with minimal temperature dependence. Notably, although the impedance slightly increases at low temperatures, it still maintains a high charge-transfer capacity and rapid ion diffusion. Then, the Zn^{2+} diffusion coefficients for PMPZ were calculated through GITT measurements to assess its electrochemical kinetics at 50 °C, 25 °C, and −50 °C. As shown in Fig. 5b and Fig. S16, PMPZ maintains a high and consistent ionic diffusion coefficient (10^{-8}–10^{-9} cm^2 s^{-1}) across different temperatures, indicating fast reaction kinetics and strong ion transport capability, further demonstrating its minimal temperature dependence. This outstanding electrochemical kinetics at low temperatures provides a foundation for developing wide-temperature AZIBs, just as shown in Fig. 5c–h.

The electrochemical performance of the PMPZ cathode was tested at selected temperatures of 50 °C, 25 °C, and −50 °C in 3 M $Zn(ClO_4)_2$ electrolyte. The PMPZ cathode delivers a high discharge capacity of 260 mA h g^{-1} (50 °C) and 175 mA h g^{-1} (−50 °C) at 0.1 A g^{-1} (Fig. 5c and d), corresponding to 110% and 75% of the discharge capacity achieved at 25 °C (233 mA h g^{-1}), respectively, while maintaining a high coulombic efficiency close to 100% at the tested temperatures. Crucially, PMPZ presents charge/discharge curves at high and low temperatures similar to those at room temperature, without obvious polarization, revealing stable electrochemical kinetics and exceptional adaptability to temperature fluctuations. After that, the cycling stability of the PMPZ cathode was evaluated at 50 °C and −50 °C. As depicted in Fig. 5e and Fig. S17, the PMPZ cathode delivers high reversible discharge capacities of 236 mA h g^{-1} (88% capacity retention) and 175 mA h g^{-1} (99% capacity retention) at 0.1 A g^{-1} after 100 cycles at 50 °C and −50 °C, respectively. Moreover, the PMPZ cathode exhibits attractive rate performance at low and high temperatures in the current density range of 0.1 to 50 A g^{-1} (Fig. 5f). At 50 °C, the capacities were 258, 238, 223, 218, 209, 200, 195, 188, and 177 mA h g^{-1} at 0.1, 0.2, 0.5, 1, 2, 5, 10, 20 and 50 A g^{-1}, respectively. Importantly, even at a low temperature (−50 °C), PMPZ still exhibits remarkable rate performance, with high discharge capacities of 176, 170, 163, 156, 148, 133, 122, 109, and 88 mA h g^{-1} at the same current density conditions. Compared with the capacities at 25 °C, the capacity retention values at −50 °C are between 50% and 80%, indicating outstanding capacity retention at low temperature. When the current density was reduced to 0.1 A g^{-1} from 50 A g^{-1}, the capacity recovered to 241 and 175 mA h g^{-1} at 50 °C and −50 °C, respectively, further confirming excellent stability and reversibility of the PMPZ cathodes at different temperatures. Subsequently, the long-term cycling stability of PMPZ cathodes at 1 A g^{-1} under the selected working temperature was evaluated, as shown in Fig. 5g. The PMPZ cathode exhibits remarkable cycling stability at 50 and −50 °C, with a high capacity of

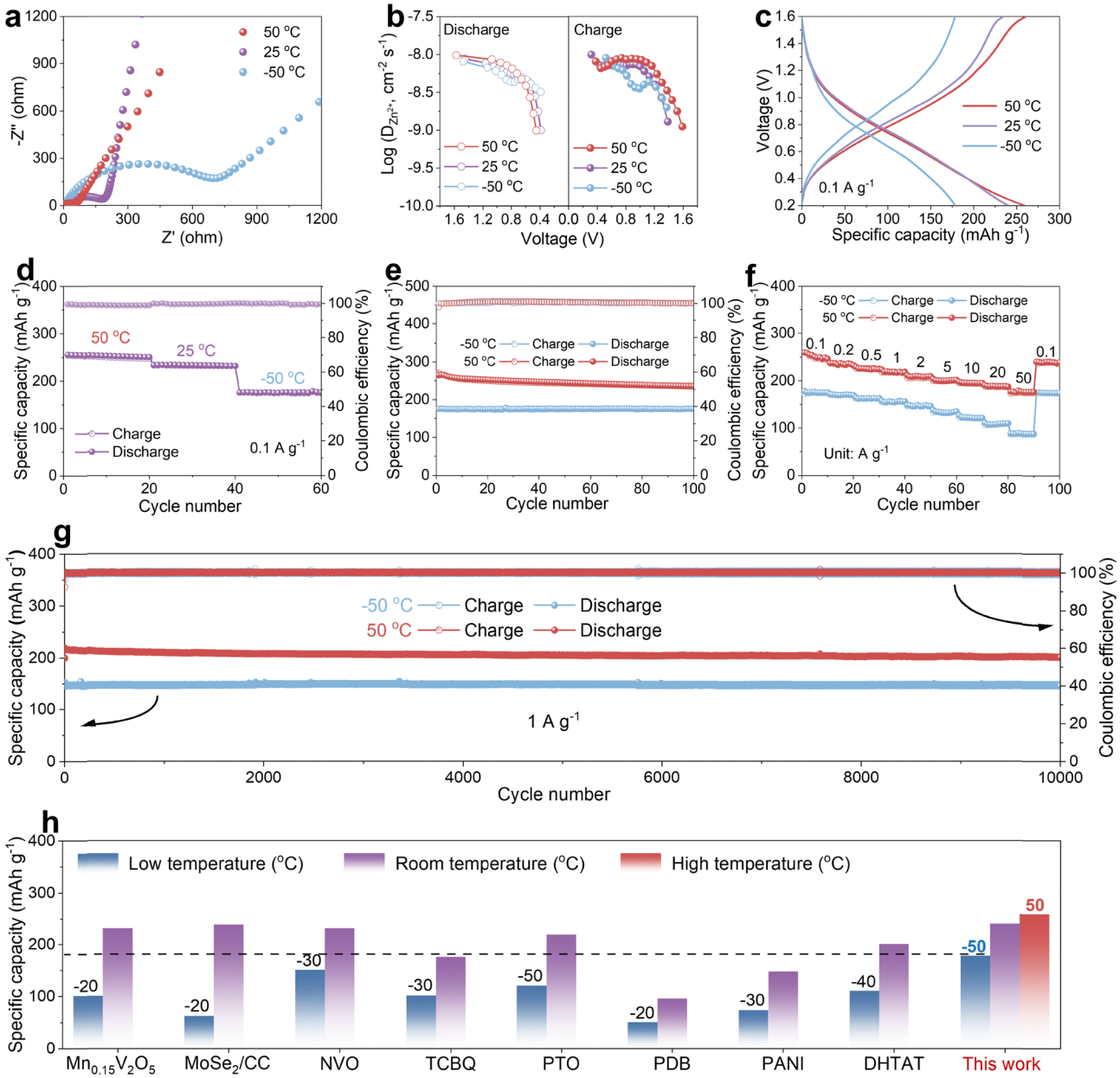

Fig. 5 Electrochemical performance of the PMPZ cathode for AZIBs at high and low temperatures. (a) EIS plots of PMPZ at 50 °C, 25 °C, and −50 °C. (b) Zn^{2+} diffusion coefficients of the PMPZ cathode at 50 °C, 25 °C, and −50 °C. (c) Typical charge/discharge curves of PMPZ at 0.1 A g^{-1} at 50 °C, 25 °C, and −50 °C. (d) Electrochemical performance of PMPZ across a wide temperature range from −50 °C to 50 °C. (e) Cycling performance of PMPZ at 0.1 A g^{-1} at 50 °C and −50 °C. (f) Rate performance of PMPZ at different current densities and at 50 °C and −50 °C. (g) Long-term cycling performance of PMPZ at 1 A g^{-1} at 50 °C and −50 °C. (h) Comparison of the specific capacity among PMPZ and previously reported cathode materials at different temperatures.

202 mA h g^{-1} (92% capacity retention) at 50 °C and an impressive capacity of 146 mA h g^{-1} (99% capacity retention) at −50 °C after 10 000 cycles. The excellent cycling stability mainly results from the extended aromatic backbone and strong intermolecular π–π interactions within the PMPZ polymer. Collectively, these results demonstrate that PMPZ exhibits superior wide-temperature performance, significantly surpassing most reported cathodes (summarized comparatively in Fig. 5h). The outstanding capacity retention, rate performance, cycling stability, and minimal polarization across an extreme temperature range (−50 °C to 50 °C) unequivocally highlight the practicality and superiority of the PMPZ cathode for AZIBs.

Electrochemical performance in a seawater-based electrolyte

The properties of natural seawater, including its abundance, eco-benignity, and negligible cost, make it an ideal electrolyte for aqueous batteries. Thus, we explored the application of a seawater-based electrolyte (3 M $Zn(ClO_4)_2$) in AZIBs (Fig. 6a). Compared to traditional deionized (DI) water-based electrolytes, the seawater-based electrolyte exhibits similar high ionic

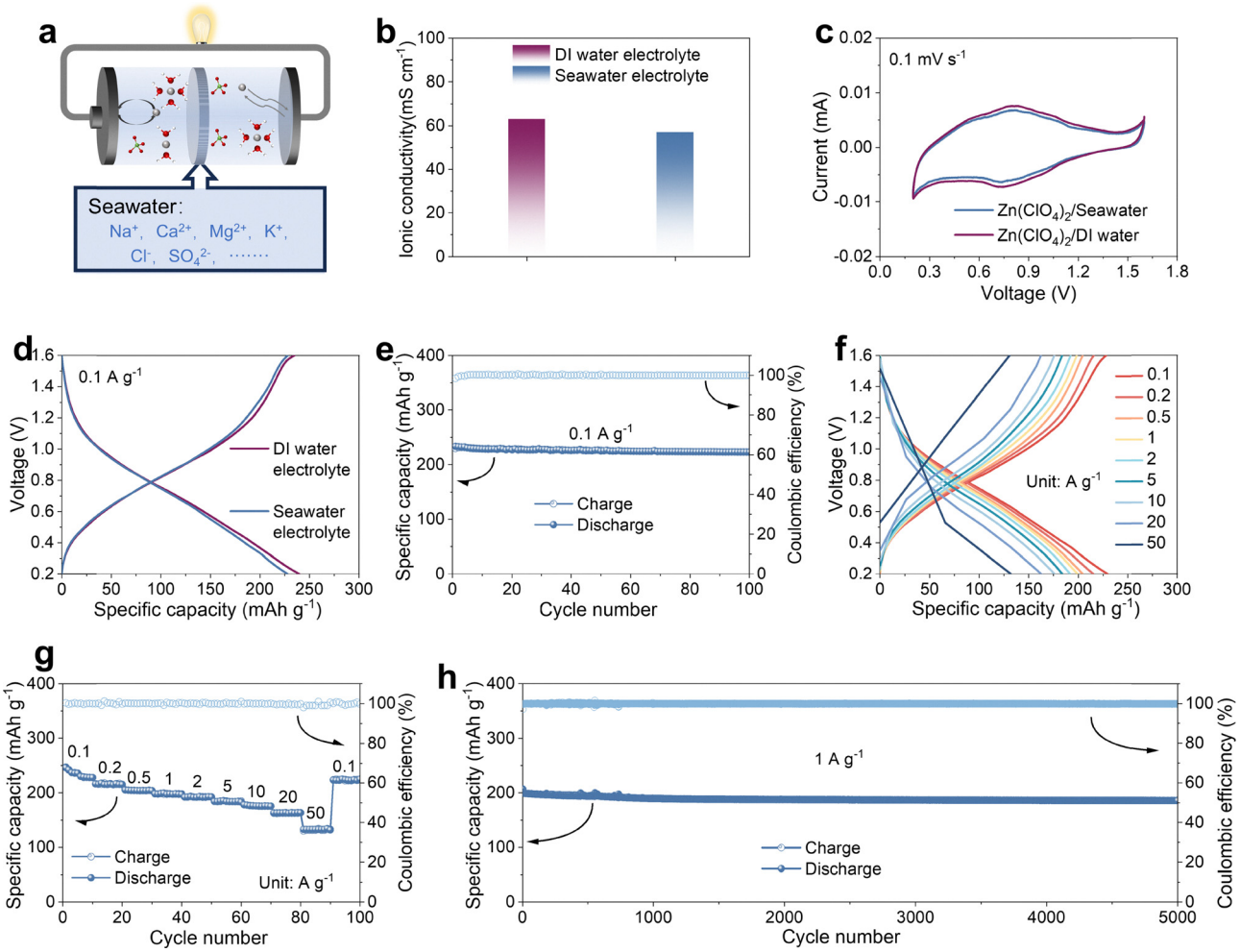

Fig. 6 Electrochemical performance of PMPZ with a seawater-based electrolyte. (a) Schematic of the Zn//PMPZ cell using a seawater-based electrolyte. (b) Ionic conductivity of the DI water-based and seawater-based electrolytes (c) CV curves of PMPZ at 0.1 mV s^{-1} with the DI water-based and seawater-based electrolytes. (d) Charge/discharge curves of PMPZ at 0.1 A g^{-1} with the DI water-based and seawater-based electrolytes. (e) Cycling performance of PMPZ at 0.1 A g^{-1} with a seawater-based electrolyte. (f) Charge/discharge curves and (g) rate performance of PMPZ at different current densities with a seawater-based electrolyte. (h) Long-term cycling stability of PMPZ at 1 A g^{-1} with a seawater-based electrolyte.

conductivity (Fig. 6b and Fig. S18), which can ensure fast reaction kinetics. However, the presence of multiple ions (Na^+, Ca^{2+}, Mg^{2+}, K^+, Cl^-, and SO_4^{2-}, *etc.*) in seawater often leads to severe interference, causing most cathodes unsuitable for applications. Therefore, developing high-performance cathode materials capable of operating in complex seawater environments remains a challenge.

The PMPZ cathode enables reversible co-insertion of multivalent and multiple ions (Zn^{2+}/H^+), demonstrating exceptional adaptability to various ionic species. When tested in a seawater-based electrolyte, the PMPZ cathode exhibits the same redox peaks and charge/discharge curves as observed in the DI water-based electrolyte (Fig. 6c and d), indicating that the complex composition of seawater does not affect the redox behavior of PMPZ. Furthermore, the Zn//PMPZ cell using the $Zn(ClO_4)_2$/seawater electrolyte exhibits a high reversible capacity of 223 mA h g^{-1} after 100 cycles at 0.1 A g^{-1}, following activation *via* 10 cycles at 1 A g^{-1} (Fig. 6e). Moreover, the PMPZ cathode demonstrates remarkable rate performance, with capacities of 230, 216, 204, 197, 192, 183, 175, 162, and 133 mA h g^{-1} at current densities of 0.1, 0.2, 0.5, 1, 2, 5, 10, 20, and 50 A g^{-1}, respectively (Fig. 6f and g), while maintaining stable charge/discharge curves at various current densities. Additionally, even after 5000 cycles, the cell retains a reversible capacity of 184 mA h g^{-1} at 1 A g^{-1} (Fig. 6h). These results highlight its outstanding energy storage performance and strong adaptability to complex seawater environments.

Conclusions

In summary, we successfully synthesized PMPZ through a one-step Friedel–Crafts reaction and employed it as a high-performance cathode for AZIBs. The optimization of electrochemical performance was achieved through strategic modulation of electron delocalization and integration of multifunctional active groups within its extended π-conjugated architecture. The heterocyclic

conjugated units within the PMPZ polymer facilitate extensive electron delocalization along the molecular backbone, resulting in significantly enhanced electron affinity and electronic conductivity. Additionally, the synergistic effect of multiple C═O and C═N groups enables efficient multi-electron redox processes *via* electron delocalization, markedly elevating the charge storage capability and reaction kinetics at different temperatures. Moreover, integrated theoretical calculations and advanced characterizations, including *operando* synchrotron spectroscopy, EQCM-D, and *ex situ* XPS, collectively verify a reversible Zn^{2+}/H^{+} co-insertion mechanism involving multi-electron transfer within this conjugated molecular system. Leveraging these synergistic advantages, the PMPZ cathode exhibits a high capacity of 240 mA h g^{-1} at 0.1 A g^{-1}, cycling stability beyond 60,000 cycles, and remarkable rate performance of 179 mA h g^{-1} at 50 A g^{-1}, even in a seawater-based electrolyte. Notably, it maintains operational stability across extreme temperatures, delivering discharge capacities of 260 mA h g^{-1} at 50 °C and 175 mA h g^{-1} at −50 °C under the current density of 0.1 A g^{-1}, with stable cycling exceeding 10 000 cycles under both conditions. Even in a seawater-based electrolyte, the PMPZ cathode exhibits a high capacity of 223 mA h g^{-1} at 0.1 A g^{-1} and maintains stable performance over 5000 cycles. This work demonstrates a molecular engineering strategy for developing high-performance organic cathode materials capable of achieving ultra-stable and high-rate AZIBs under harsh operating conditions.

Author contributions

Q. Ma and C. Ji contributed equally to this work. C.Z. and D.C. conceived the idea and designed the experiments. Q.M. and C. Ji conducted the material characterization and electrochemical measurements. Y.X., Z.W., L.Z., and R.W. assisted with the electrochemical measurements and data analysis. H.L. performed the DFT calculations. Q.Z. commented on the paper. Q. M. and C.Z. co-wrote the manuscript. All authors discussed and analyzed the results.

Conflicts of interest

The authors declare no conflicts of interest.

Data availability

The data supporting this article have been included as part of the supplementary information (SI). Supplementary information is available, which includes the experimental methods, additional material characterization, and electrochemical performance. See DOI: https://doi.org/10.1039/d6ee00199h.

Acknowledgements

This work is supported by the National Key R&D Project (2024YFE0101100) under its Singapore-China Joint Flagship Project (Clean Energy), the National Natural Science Foundation of China (U24A2060, 52172173, and 52302205), the Excellent Research and Innovation Team Project of Anhui Province (2022AH010001), the Fundamental Research Funds for the Central Universities (20720250005), and the Science and Technology Commission of Shanghai Municipality (25DZ3002901, 2024ZDSYS02, and 25PY2600100). The authors also acknowledge the Anhui Postdoctoral Scientific Research Program Foundation (2025A1029), the Postdoctoral Fellowship Program of CPSF under Grant (GZC20250098), the China Postdoctoral Science Foundation (2025M770135) and the China Postdoctoral Science Foundation-Anhui Joint Support Program (2024T013AH). We also thank the infrared spectroscopy and micro spectroscopy beamline (BL01B) facility at the National Synchrotron Radiation Laboratory (NSRL) for the help in characterization.

References

1 K. Hua, Q. Ma, Y. Liu, P. Xiong, R. Wang, L. Yuan, J. Hao, L. Zhang and C. Zhang, *ACS Nano*, 2025, **19**, 14249–14261.
2 X. Zhang, R. Wang, Z. Liu, Q. Ma, H. Li, Y. Liu, J. Hao, S. Zhang, J. Mao and C. Zhang, *Adv. Energy Mater.*, 2024, **14**, 2400314.
3 C. Zhang, S. Chou, Z. Guo and S. X. Dou, *Adv. Funct. Mater.*, 2024, **34**, 2308001.
4 Z. Mao, H. Wang, T. Zhang, Y. Wang, W. Zhou and D. Chao, *J. Am. Chem. Soc.*, 2025, **147**, 34059–34069.
5 R. Wang, Y. Liu, Q. Luo, P. Xiong, X. Xie, K. Zhou, W. Zhang, L. Zhang, H. J. Fan and C. Zhang, *Adv. Mater.*, 2025, **37**, 2419502.
6 Y. Liu, L. Zhang, L. Liu, Q. Ma, R. Wang, P. Xiong, H. Li, S. Zhang, J. Hao and C. Zhang, *Adv. Mater.*, 2025, **37**, 2415979.
7 Y. Liu, F. Li, J. Hao, H. Li, S. Zhang, J. Mao, T. Zhou, R. Wang, L. Zhang and C. Zhang, *Adv. Funct. Mater.*, 2024, **34**, 2400517.
8 R. Wang, Q. Ma, L. Zhang, Z. Liu, J. Wan, J. Mao, H. Li, S. Zhang, J. Hao, L. Zhang and C. Zhang, *Adv. Energy Mater.*, 2023, **13**, 2302543.
9 W. Zhang, Y. Liu, X. Luo, R. Wang, K. Zhou, L. Yuan, F. Li, H. Li, L. Zhang and C. Zhang, *Adv. Funct. Mater.*, 2025, **35**, e12633.
10 W. Zhou, M. Song, P. Liang, X. Li, X. Liu, H. Li, T. Zhang, B. Wang, R. Zhao, Z. Zhao, W. Li, D. Zhao and D. Chao, *J. Am. Chem. Soc.*, 2023, **145**, 10880–10889.
11 R. Wang, S. Xin, D. Chao, Z. Liu, J. Wan, P. Xiong, Q. Luo, K. Hua, J. Hao and C. Zhang, *Adv. Funct. Mater.*, 2022, **32**, 2207751.
12 X. Luo, L. Jiao, D. Chao, F. Li, R. Wang, S. Zhang, Q. Ma, H. Li, L. Zhang and C. Zhang, *Angew. Chem., Int. Ed.*, 2025, **64**, e202514375.
13 J. Zhu, Q. Zhou, L. Wang, W. Zhou, M. Chen, X. Liu, D. Gao and D. Chao, *Adv. Energy Mater.*, 2024, **14**, 2304554.
14 X. Xie, R. Wang, L. Jiao, H. Li, L. Yuan, S. Zhang, J. Mao and C. Zhang, *Sci. China Chem.*, 2026, DOI: 10.1007/s11426-025-3093-8.

15 H. Jin, D. Zhao and D. Chao, *Joule*, 2025, **9**, 101917.
16 L. Zhao, Y. Jia, Y. Wu, T. Gu, X. Zhou, X. Wang, L. Zhong, S. Zhan, H. Lv, C. Zhi and J. Liu, *Angew. Chem., Int. Ed.*, 2025, **64**, e202425082.
17 Z. Song, L. Miao, H. Duan, Y. Lv, L. Gan and M. Liu, *Angew. Chem., Int. Ed.*, 2024, **63**, e202401049.
18 H. Li, M. Cao, R. Wang, P. Xiong, Y. Liu, L. Zhang, L. Zhang, L. Zhang, D. Chao and C. Zhang, *Angew. Chem., Int. Ed.*, 2025, **64**, e202508057.
19 G. Yang, Y. Zhu, Q. Zhao, Z. Hao, Y. Lu, Q. Zhao and J. Chen, *Sci. China Chem.*, 2023, **67**, 137–164.
20 Y. Wang, W. Zhang, J. Yang, Y. Gong, J. Zhang, M. Fang, Q.-H. Yang and Z. Li, *Matter*, 2022, **5**, 4467–4479.
21 X. Chen, Y. Ma, Y. Lu, H. Zhang, B. Yang and Q. Liu, *Chin. Chem. Lett.*, 2026, **37**, 110666.
22 W. Wang, S. Zhang, L. Zhang, R. Wang, Q. Ma, H. Li, J. Hao, T. Zhou, J. Mao and C. Zhang, *Adv. Mater.*, 2024, **36**, 2400642.
23 L. Zhang, R. Wang, Z. Liu, J. Wan, S. Zhang, S. Wang, K. Hua, X. Liu, X. Zhou, X. Luo, X. Zhang, M. Cao, H. Kang, C. Zhang and Z. Guo, *Adv. Mater.*, 2023, **35**, 2210082.
24 Q. Q. Sun, T. Sun, J. Y. Du, K. Li, H. M. Xie, G. Huang and X. B. Zhang, *Adv. Mater.*, 2023, **35**, 2301088.
25 Z. Li, J. Tan, Y. Wang, C. Gao, Y. Wang, M. Ye and J. Shen, *Energy Environ. Sci.*, 2023, **16**, 2398–2431.
26 T. Chen, Y. Zou, Y. Xu, P. Chen, S. Zeng, K. Hua, H. Liu, Y. Zhou, L. Zhang and C. Zhang, *Chin. Chem. Lett.*, 2025, 111869.
27 R. Wang, Y. Zhang, C. Ma, X. Wang, M. Cai, H. Du, Z. Yang, D. Chao and Y. Wang, *Adv. Funct. Mater.*, 2025, **35**, 2505318.
28 S. Tang, C. Ye and X. Zhou, *Angew. Chem., Int. Ed.*, 2025, **64**, e202501743.
29 W. Li, H. Xu, H. Zhang, F. Wei, L. Huang, S. Ke, J. Fu, C. Jing, J. Cheng and S. Liu, *Nat. Commun.*, 2023, **14**, 5235.
30 P. Bao, L. Cheng, X. Yan, X. Nie, X. Su, H. G. Wang and L. Chen, *Angew. Chem., Int. Ed.*, 2024, **63**, e202405168.
31 T. Sun, W. Zhang, Z. Zha, M. Cheng, D. Li and Z. Tao, *Energy Storage Mater.*, 2023, **59**, 102778.
32 X. Peng, A. Baktash, N. Alghamdi, M. M. Rana, Y. Huang, X. Hu, C. He, Z. Luo, J. Ning, L. Wang and B. Luo, *Adv. Energy Mater.*, 2024, **14**, 2400147.
33 L. Lin, Z. Lin, J. Zhu, K. Wang, W. Wu, T. Qiu and X. Sun, *Energy Environ. Sci.*, 2023, **16**, 89–96.
34 F. Ye, Q. Liu, H. Dong, K. Guan, Z. Chen, N. Ju and L. Hu, *Angew. Chem., Int. Ed.*, 2022, **61**, e202214244.
35 K. Zhou, H. Yan, Q. Tang, Z. Luo, X. Wang and F. Cai, *J. Power Sources*, 2024, **591**, 233854.
36 L. Zhong, C. Liu, Y. Zhang, J. Li, F. Yang, Z. Zhang and D. Yu, *Angew. Chem., Int. Ed.*, 2024, **64**, e202413971.
37 L. Zhong, C. Wang, J. He, Z. Lin, X. Yang, R. Li, S. Zhan, L. Zhao, D. Wu, H. Chen, Z. Tang, C. ZHi and H. Lv, *Adv. Mater.*, 2024, **36**, 2314050.
38 J. Wang, X. Zhang, Z. Liu, J. Yu, H. G. Wang, X. L. Wu, F. Cui and G. Zhu, *Angew. Chem., Int. Ed.*, 2024, **63**, e202401559.
39 R. Wang, J. He, C. Yan, R. Jing, Y. Zhao, J. Yang, M. Shi and X. Yan, *Adv. Mater.*, 2024, **36**, 2402681.
40 Y. Zhang, Q. Huang, Z. Song, L. Miao, Y. Lv, L. Gan and M. Liu, *Adv. Funct. Mater.*, 2024, **35**, 2416415.
41 T. Sun, Z. Yi, W. Zhang, Q. Nian, H. J. Fan and Z. Tao, *Adv. Funct. Mater.*, 2023, **33**, 2306675.
42 X. Liu, J. Tang, D. Bin, Y. Wang, C. Li, L. Su, Y. Shen, W. Hu, Z. Hu, W. Zhuang, B. Yang, H. Lu and Y. Wang, *Energy Storage Mater.*, 2025, **81**, 104517.
43 T. Sun, W. Zhang, Q. Nian and Z. Tao, *Chem. Eng. J.*, 2023, **452**, 139324.
44 T. Chen, H. Banda, L. Yang, J. Li, Y. Zhang, R. Parenti and M. Dincă, *Joule*, 2023, **7**, 986–1002.
45 H. Dai, L. Guan, M. Mao and C. Wang, *Nat. Rev. Clean Technol.*, 2025, **1**, 493–510.
46 Y. Zhang, M. Li, Z. Li, Y. Lu, H. Li, J. Liang, X. Hu, L. Zhang, K. Ding, Q. Xu, H. Liu and Y. Wang, *Angew. Chem., Int. Ed.*, 2024, **63**, e202410342.
47 J. Ning, X. Zhang, D. Xie, Q. He, J. Hu, J. Tang, R. Li, H. Meng and K. X. Yao, *Angew. Chem., Int. Ed.*, 2024, **63**, e202319796.
48 D. Du, J. Zhou, Z. Yin, G. Feng, W. Ji, H. Huang and S. Pang, *Adv. Energy Mater.*, 2024, **14**, 2400580.
49 L. Yan, Q. Zhu, Y. Qi, J. Xu, Y. Peng, J. Shu, J. Ma and Y. Wang, *Angew. Chem., Int. Ed.*, 2022, **61**, e202211107.
50 X. Wang, J. Tang and W. Tang, *Adv. Funct. Mater.*, 2022, **32**, 2200517.
51 X. Yu, K. Zhou, C. Liu, J. Li, J. Ma, L. Yan, Z. Guo and Y. Wang, *Angew. Chem., Int. Ed.*, 2025, **64**, e202501359.
52 Z. Yang, P. Meng, M. Jiang, X. Zhang, J. Zhang and C. Fu, *Angew. Chem., Int. Ed.*, 2024, **63**, e202403424.
53 C. Ding, Y. Zhao, W. Yin, F. Kang, W. Huang and Q. Zhang, *Angew. Chem., Int. Ed.*, 2024, **64**, e202417988.
54 H. Cui, D. Zhang, Z. Wu, J. Zhu, P. Li, C. Li, Y. Hou, R. Zhang, X. Wang, X. Jin, S. Bai and C. Zhi, *Energy Environ. Sci.*, 2024, **17**, 114–122.
55 J. Yang, H. Hua, H. Yang, P. Lai, M. Zhang, Z. Lv, Z. Wen, C. C. Li, J. Zhao and Y. Yang, *Adv. Energy Mater.*, 2023, **13**, 2204005.
56 Y. Chen, J. Li, Q. Zhu, K. Fan, Y. Cao, G. Zhang, C. Zhang, Y. Gao, J. Zou, T. Zhai and C. Wang, *Angew. Chem., Int. Ed.*, 2022, **61**, e202116289.
57 H. Li, M. Cao, Z. Fu, Q. Ma, L. Zhang, R. Wang, F. Liang, T. Zhou and C. Zhang, *Chem. Sci.*, 2024, **15**, 4341–4348.
58 D. Wang, M. Qin, C. Zhang, M. Li, C. Peng, C. Zhi, Q. Li and L. Zhu, *Chem. Sci.*, 2025, **16**, 3630–3637.
59 L. Zhang, Y. Zhang, X. Wang, X. Wang, Q. Wang, J. Li, Z. Li, K. Ding, Y. Peng, H. Liu and Y. Wang, *Adv. Funct. Mater.*, 2025, **36**, e13189.
60 J. Hao, S. Zhang, H. Wu, L. Yuan, K. Davey and S.-Z. Qiao, *Chem. Soc. Rev.*, 2024, **53**, 4312–4332.

